ROYAL AERONAUTICAL SOCIETY

REGULAR PAPER

A folding wing system for guided ammunitions: mechanism design, manufacturing and real-time results with LQR, LQI, SMC and SOSMC

A. Sayıl[1] , F. Erden[2] , A. Tüzün[3] , B. Baykara[3] and M. Aydemir[3]

[1]Department of Astronautical Engineering, Sivas University of Science and Technology, Sivas 58000, Türkiye, [2]Department of Aeronautical Engineering, Sivas University of Science and Technology, Sivas 58000, Türkiye and [3]Department of Mechatronic Systems, TUBITAK Defense Industries Research and Development Institute – SAGE, Ankara 06261, Türkiye
Corresponding authors: F. Erden and A. Tüzün; Emails: fuaterden@sivas.edu.tr; aydin.tuzun@tubitak.gov.tr

Abstract

In the present work, a folding wing system (FWS) was developed for guided ammunitions, so that the swept-back angle could be adjusted during both gliding and diving phases. Unlike previous designs, the FWS does not have any fixing mechanisms or brake elements, and it provides folding functionality to reduce the drag force during the terminal phase. We conducted mechanism design, manufactured the FWS, performed system identification and designed various controllers including linear quadratic regulator (LQR), linear quadratic integrator (LQI), sliding mode control (SMC) and second-order sliding mode control (SOSMC) to adjust and hold the desired swept-back angles. Then, the performance of the FWS was tested experimentally under two different flight scenarios, with and without aerodynamic loads. While all controllers operated with almost zero steady-state error (SSE) in the absence of aerodynamic loads, the SOSMC was the most effective controller under aerodynamic loads, considering SSE, delay, chattering, and energy consumption.

Nomenclature

L_2,	distance between wing hinge to link hinge
L_3,	length of connection rod
c,	eccentricity
θ_2,	wing angle
θ_3,	connection rod angle
$\dot{\theta}_2$,	angular velocity of wing (L_2)
$\dot{\theta}_3$	angular velocity of connection rod (L_3)
s,	slider position
$\dot{s}$,	velocity of slider
$N_{velocity}$,	transmission ratio
$\dot{\theta}_{motor}$,	angular velocity of motor
p,	screw pitch
i,	reducer ratio
K_t,	torque constant of motor
J_{eq},	equivalent moment of inertia of FWS reduced to motor
i,	motor current
B_{eq},	equivalent viscous friction of the system reduced to motor.
$y(t)$,	measured noisy output
n_u,	number of input channel

n_k,	input delay
u(t),	controlled input
e(t),	white noise
q^{-1},	time shift operator
x(t),	state vector
u(t),	input vector
K_{LQR},	LQR gain matrix
J,	cost function
$V,\ \dot{V},\ \ddot{V}$,	Lyapunov function and its derivatives
$\Delta A, \Delta B, \Delta C$,	unknown model uncertainties
d(t),	external disturbance of the system
$D\,(t, u(t))$,	lumped uncertainty
D_{max},	upper bound for the uncertainty
s,	sliding surface variable
$e, \dot{e}, \ddot{e}$,	tracking error and its derivatives
$x_d, \dot{x}_d, \ddot{x}_d$,	desired position and its derivatives
u,	control signal
u_{eq},	equivalent control switching control
u_{sw},	switching control
$\lambda, \lambda_2,\ k,\ k_s$,	positive independent parameter gains
β_c,	gain parameter of sliding surface

1.0 Introduction

Smart systems are ushering in a new era with developing technology and are widely used now in various applications including military. For instance, low-cost smart ammunitions are providing battle superiority thanks to their excellent precision and high reliability [1–3]. In the past, general-purpose bombs which are launched from aircrafts and approach their target primarily via gravity, lacked target-seeking and/or guidance features, and thus had limited precision [1, 4]. The development of guidance kits transformed these once-unguided free-fall bombs to efficient, reliable and deadly air-to-ground smart ammunitions [5]. In fact, various guidance kits have been developed to date such as laser guidance and precision guidance [4, 6–8]. However, maximum range of general-purpose bombs are still limited due to lack of propulsion, and guidance kits won't offer a solution to this drawback [5, 9–11]. This problem can be resolved by attaching a wing kit to the ammunition, such as in the case of Joint Direct Attack Munition-Extended Range (JDAM-ER) or Wing-Assisted Guidance Kit (WGK) [11–13]. In the previous wing kits, the wings are fixed at a predetermined optimum angle, shortly following the launch of ammunition [14–25]. They could operate only in one direction and as the term fixed implies, previous designs won't allow to change the swept-back angle anymore once the wings are fixed at the predetermined angle. Even though the fixed wings increase the maximum range during the gliding phase, they could also cause extra drag force during diving towards the target. This drag force causes the bomb to slow down, reducing its destructive power, and creates a drag moment on the wings [26]. In fact, the guidance kit might balance this moment up to a point by creating a counter moment. Yet, this momentum still could cause the angle-of-attack to change, limiting the accuracy and precision [27].

To solve this, we developed a folding wing system (FWS) with an adjustable swept-back angle feature in the present work. The idea is to design and develop a folding mechanism and a controller, which could change the swept-back angle both during the gliding and diving phases. By this way, the swept-back angle could be adjusted to 90° (wing closed position) during the diving phase to eliminate the drag force, and thus will minimise the risk of any change in the angle-of-attack. Besides, the proposed mechanism could also be used in continuously adjusting the swept-back angle during the gliding phase to maximise precision and accuracy. In addition to this, our system could be used in adapting the ammunition to any environmental or unforeseen disturbances that could arise during a mission. Besides, such a system could also be adapted in the future to loitering ammunitions. It is known that there are currently

six main configurations exist for loitering ammunitions, namely conventional fixed-wing, canard, delta wing, cruciform wing, tandem wing and rotorcraft [28]. However, none of them provides two-directional movement of wings during the flight. Overall, the main contributions of this work are that this is the first paper on the development of a wing kit with a foldable feature, which could provide many advantages over conventional designs as mentioned previously. Also, this work could help to develop various loitering ammunition designs with folding functionality in the future.

In this work, design parameters, controller parameters and flight scenarios for specific general-purpose bombs were used based on the expertise of an institute working on development of bombs and such kits for about 50 years. Briefly, we designed a slider-crank mechanism driven by a brushless direct current (BLDC) motor. The folding wings are actuated through a connection rod upon movement of the slider on the longitudinal axis. In contrast to previous wing kits, the as-developed FWS provides a folding functionality and there are not any fixing mechanisms or brake elements for fixing of wing position. Instead, controllers were designed to adjust and hold the desired swept-back angles. Naturally, the air conditions would not be static during any mission, and thus, as-developed FWS should actually be capable of adapting to a dynamic environment. To ensure this, we compared the performances of linear and nonlinear controllers under various aerodynamic loads for a specific flight scenario. Overall, linear quadratic regulator (LQR), linear quadratic integrator (LQI), sliding mode control (SMC) and second-order sliding mode control (SOSMC) algorithms were implemented to adjust the swept-back angle through BLDC motor position. We report that while all controllers followed the reference input precisely in the absence of aerodynamic disturbances, the chattering phenomenon was observed in the case of SMC. Regarding the flight scenario with aerodynamic disturbances, LQI, SMC and SOSMC performed efficiently with a nearly zero steady-state error (SSE) (0.01°, 0.05°, 0.05°, respectively), while LQR performed with a 0.39° SSE. Also, it is worth mentioning that all results are obtained with the physical FWS in real-time.

2.0 Materials and methods

The present work involves a mechanism design, then material selection, manufacturing of all components and assembling of the proposed FWS. Following this, system identification and controller design were conducted. Finally, controller performances were tested under two different flight scenarios (one with aerodynamic loads, and one without aerodynamic loads). All of these steps are explained in detail through this section.

2.1 Mechanism design and system modelling

When starting the conceptual design of a wing kit, firstly, a designer should consider how ammunitions, particularly the ones with a wing kit, are carried in fighter aircrafts. In fact, ammunitions with a wing kit attachment can only be stored in fighter aircrafts when the wings are at their closed position, or in other words when the swept-back angle is 90° [29, 30]. Previous wing kits are designed in such a way that they could operate only one-time and one-direction to reach a fixed swept-back angle after the ammunition is launched from the aircraft as afore-mentioned in the introduction section [5]. These systems are mostly driven by a pulley, an electromechanical actuator or piston member (i.e., pneumatic, pyrotechnic-based, hydraulic) to adjust and lock the wings [14–25, 31–33]. However, pulleys or pre-compressed tension springs need to be installed again for any reverse direction movements. For piston driven systems, an extra gas tank is necessary for the similar purpose. In other words, it is simply not possible to control the wings in two-directions with current wing kit designs, unless these improvements are implemented. On the other hand, these additions would inevitably increase the cost and complicate the mechanisms, as well as necessitating extra space. Instead of these, the proposed FWS mechanism could drive the wings in two directions by a BLDC motor. The electromechanical actuator (BLDC motor) could change the direction through changing the sign of current, and thus, the swept-back angle could easily be adjusted to reach any desired position during the flight without the necessity of any brake or fixing mechanisms.
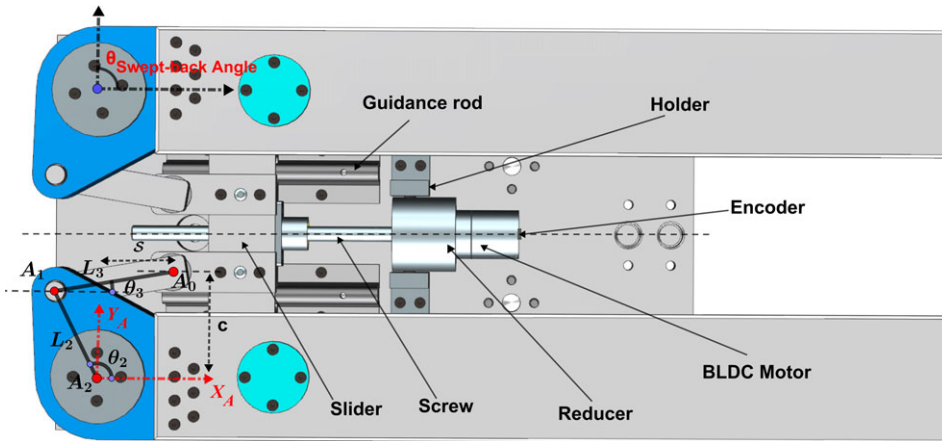
Figure 1. *CAD design of the FWS at 90° swept-back angle: components and mechanism illustration.*

In this study, working conditions were chosen as 40°–90° for swept-back angle, 1 s for time elapsed to open/close the wings, and two flight scenarios were considered with and without external loads on wings. In other words, the FWS considered here must open/close the wings from 40° to 90° (and vice versa) in 1 s and can operate under aerodynamic disturbances. A slider-crank mechanism was designed to fulfill these requirements, and the FWS contains a screw for slider movement, as well as twin connection rods to pull the wings as can be seen in Fig. 1. The FWS was designed with symmetrical connection rods and wings that rotate in reverse directions to balance the inertia and moments generated during the wing rotation process, and hence, minimising any adverse effects on flight stability. The motor assembly was put inside a casing and mounted through screw to the FWS. The connection rods were connected to the slider and wings by revolute joints. Link dimensions and eccentricity were optimised through the closed-loop equation to minimise control torque and mechanism stroke. The closed-loop equation Equation (1) and its derivative Equation (2) are:

$$s + ic = L_2 e^{i\theta_2} + L_3 e^{i\theta_3} \tag{1}$$

$$\dot{s} = L_2 \dot{\theta}_2 e^{i\theta_2} + L_3 \dot{\theta}_3 e^{i\theta_3} \tag{2}$$

where L_2, L_3, c, θ_2, θ_3, $\dot{\theta}_2$, $\dot{\theta}_3$, s and $\dot{s}$ are the distance between wing hinge to link hinge, length of connection rod, eccentricity, wing angle, connection rod angle, angular velocity of wing (L_2), angular velocity of connection rod (L_3), slider position and velocity of slider, respectively (Fig. 1). When wing position changes from closed to open or vice versa, the relationship between the position and the velocity of each mechanism components and the swept-back angle is shown in Fig. 2.

In mechanism design, it is important to consider the mechanism transmission ratio, which defines the relation between input and output [34]. Regarding the transmission ratio of the FWS developed in this work, it represents the relation between angular velocity of motor and angular velocity of wings, and can be calculated by Equation (3):

$$N_{velocity} = \frac{\dot{\theta}_{motor}}{\dot{\theta}_2} = \frac{2\pi i}{p} L_2 \frac{sin(\theta_2 - \theta_3)}{cos(\theta_3)} \tag{3}$$

where $N_{velocity}$ is the transmission ratio, $\dot{\theta}_{motor}$ is the angular velocity of motor, p is the screw pitch and i is the reducer ratio.

For convenience, the motor position (θ_{motor}) is divided by $N_{velocity}$ to calculate the actual rotation of wings. The mean of $N_{velocity}$ was found to be 671 by averaging it for different swept-back angle values as depicted in Fig. 3a. Briefly, it implies that when the motor completes about 1.86 turns (671° rotation), the wing swept-back angle is changed by 1 degree. Figure 3b illustrates the relation between the motor torque and swept-back angle to adjust opened position (40°) in 1 s under varying loads. The aerodynamic
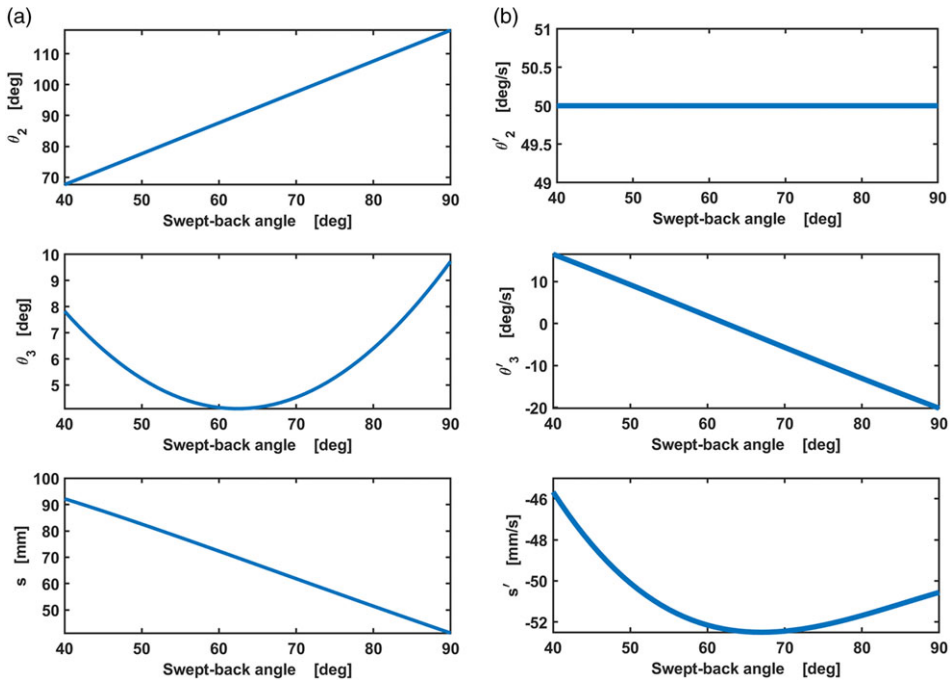
Figure 2. *Changes in the swept-back angle versus position (a), and velocity (b) of each mechanism links.*

disturbance on the wings is increasing with swept-back angle, and thus higher motor torques are required to reach higher angles, as expected. Also, Fig. 3b shows normalised motor rpm values with respect to maximum motor rpm and as can be seen, the normalised values increase to some point, after that starting to decrease due to the behaviour of the slider-crank mechanism [35, 36].

Following the mechanical design, approximately 40 different components are produced to assemble the proposed FWS. As the proposed kit is designed to be used in guided ammunitions, structural components are manufactured from aluminum due to its optimum weight and mechanical properties [37]. Transmission parts are manufactured from stainless steel due to its excellent wear resistance. The photographs of the as-manufactured FWS with 40° and 90° swept-back angle are given in Fig. 4 for better illustration.

To evaluate the system dynamics, the mathematical model of the FWS is required. Since the current controlled BLDC motor driver is utilised in the present work, the system transfer function should be established between the applied current function and the measured motor positions. BLDC motor is modelled based on the assumptions that stator and rotor reluctance angles are not changing, power semiconductor devices are ideal, mechanical components are rigid, iron losses are negligible and the motor is unsaturated [38–41]. In this case, there should be a linear relationship between output torque τ and current i through the windings, $\tau = K_t i$ [38–41]. The dynamic equation of the FWS, and its Laplace transform are given in Equation (4), (5) and (6):

$$J_{eq}.\ddot{\theta}_{motor}(t) + B_{eq}.\dot{\theta}_{motor}(t) = \tau_{motor} = K_t.i_{motor}(t) \tag{4}$$

$$J_{eq}.\theta_{motor}(s).s^2 + B_{eq}.\theta_{motor}(s).s = .K_t.I_{motor}(s) \tag{5}$$

$$\frac{\theta_{motor}(s)}{I_{motor}(s)} = \frac{K_t}{J_{eq}.s^2 + B_{eq}.s} = \frac{\dfrac{K_t}{B_{eq}}}{\dfrac{J_{eq}}{B_{eq}}.s^2 + s} \tag{6}$$
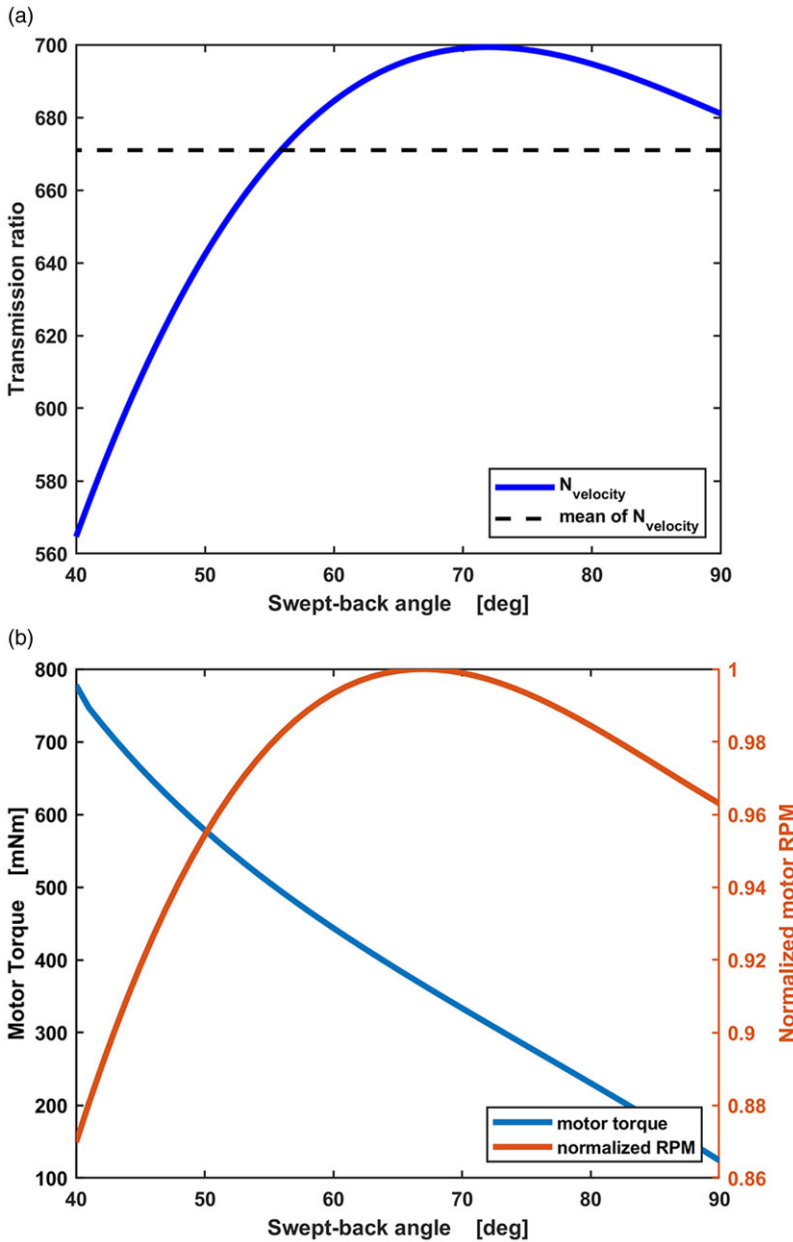
Figure 3. *Changing of transmission ratio (a), and motor torque under load (b) with swept-back angle.*

where K_t is torque constant of the motor, J_{eq} is the equivalent moment of inertia of FWS reduced to motor, i is motor current and B_{eq} is equivalent viscous friction of the system reduced to motor. Following this, the relationship between motor current and swept-back angle is defined as a transfer function in Equation (7):

$$G_{plant}\,(s) = \frac{\dfrac{\theta_{motor}\,(s)}{N_{velocity}}}{I_{motor}\,(s)} = \frac{\theta_2\,(s)}{I_{motor}\,(s)} = \frac{\dfrac{K_t}{N_{velocity}}}{J_{eq}.s^2 + B_{eq}.s} = \frac{\dfrac{K_t}{N_{velocity}B_{eq}}}{\dfrac{J_{eq}}{B_{eq}}.s^2 + s} \qquad (7)$$
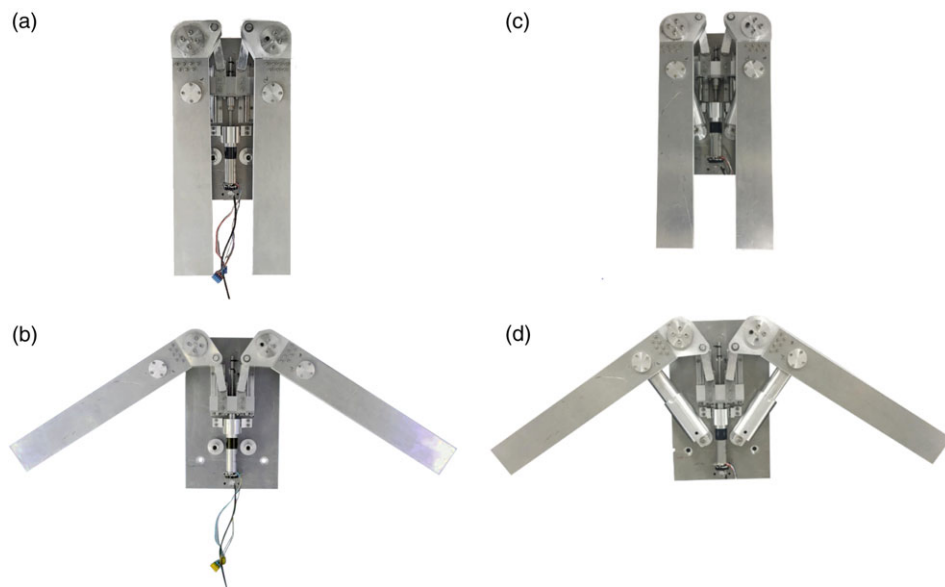
Figure 4. *Photographs of the FWS: the swept-back angle is 90° (a and c), and 40° (b and d) in the absence (a and b) and presence (c and d) of aerodynamic loads.*

2.2 System identification

System identification is a technique that converts physical systems or processes to mathematical models by obtaining experimental data through sending various signals. These mathematical models are used in control system design, fault detection, estimation of system characteristics and understanding of system dynamics [42]. In fact, a proper selection of the input signal increases the model prediction accuracy. There are various input signals that could be used to utilise for the identification of a system, including chirp, multi-sine, pseudo random binary sequence (PRBS) and impulse [43, 44]. Among them, PRBS is a popular input signal for system identification due to its simplicity [45, 46]. It involves a sequence of step functions that could be utilised in a wide range of frequencies. Therefore, PRBS signal was selected in the present work to excite physical FWS system dynamics.

The PRBS signal excited the physical FWS for the identification process and the system was assumed as a grey box system. Besides, the model orders were known through the dynamic equation of the FWS. The amplitude of PRBS was arranged as 2A since our preliminary studies show that 2A amplitude allows the slider to go through the entire mechanism stroke.

Regarding estimation of the system models, Box-Jenkins (BJ) is one of the most widely used techniques to develop reliable models in system identification [46, 47]. One of the advantages of using a BJ model is that it provides better predictions for closed-loop models [48]. During identification of the system, some problems might be encountered that make the model estimation worse. For example, if the noise model has the same poles as the system model, the sensor measurement noise might resemble the actual input signal, and thus, making it difficult to correctly estimate the plant states [49]. Using the BJ method helps to avoid such risks, because the noise and the process are modelled independently in the BJ model structure [49]. The BJ model is structured as a discrete-time transfer function with noise integration model and given in Equation (8) [50–52]:

$$y(t) = \sum_{i=1}^{n_u} \frac{B_i(q)}{F_i(q)} u(t - nk_i) + \frac{C(q)}{D(q)(1 - q^{-1})} e(t) \tag{8}$$

where y(t) is the measured noisy output, n_u is the number of input channel, n_k is the input delay, u(t) is a controlled input, e(t) is white noise, $\frac{1}{1-q^{-1}}$ is the integrator in noise channel, and B, C, D and F are

polynomial variables expressed in time shift operator, q^{-1}. Also, orders of the BJ model $\left(n_b, \ n_c, \ n_d, \ n_f\right)$ are defined as [50–52]:

$$n_b: B\left(q\right) = b_1 + b_2 q^{-1} + \ldots + b_{n_b} q^{-n_b + 1} \tag{9}$$

$$n_c: C\left(q\right) = 1 + c_1 q^{-1} + \ldots + c_{n_c} q^{-n_c}$$

$$n_f: F\left(q\right) = 1 + f_1 q^{-1} + \ldots + f_{n_f} q^{-n_f}$$

$$n_d: D\left(q\right) = 1 + d_1 q^{-1} + \ldots + d_{n_d} q^{-n_d}$$

$$\left[\,n_b\ n_c\ n_d\ n_f\ n_k\,\right] = \left[\,1\ 4\ 4\ 2\ 1\,\right] \tag{10}$$

A coefficient vector is defined to represent Box–Jenkins model orders and delays [51]. This vector must consist of positive integers. We determined the coefficient vector of our BJ model iteratively through goodness of fit and mean squared error criteria as given in Equation (10). Therefore, the resultant vector suggests that we have a total of 11 coefficients (b1, c1, c2, c3, c4, f1, f2, f3, f4, d1, d2).

2.3 Controller design

The controller of the developed FWS was designed to control the swept-back angle and adjust the desired position in a short time. Simply, position error is calculated using an encoder and reference angle. Then, position error is used as an input of our controller. The controller provides a current signal as its output. The motor driver converts this signal to a proper current, which becomes the input of our BLDC motor. In this work, LQR, LQI, SMC and SOSMC are designed, and their real-time results are compared.

LQR is a widely used optima l control technique in practical engineering, and thus it is chosen for performing the precision position control of FWS. It seeks a controller that could minimise the cost function, J, as given in Equation (13). LQR takes the states of the dynamical system and control input into account to make optimal control decisions using two positive definite matrices, which are called Q and R. In fact, the elements of these matrices can be adjusted by designers to better satisfy the system requirements. Q matrix penalises the departure of system states, while R matrix penalises the control input [53]. The state space model of the system is defined as below:

$$\dot{x}(t) = Ax(t) + Bu(t) = \begin{bmatrix} 0 & 1 \\ 0 & \dfrac{-B_{eq}}{J_{eq}} \end{bmatrix} x(t) + \begin{bmatrix} 0 \\ \dfrac{K_t}{B_{eq}} \end{bmatrix} i(t) \qquad t \geq 0, \quad x\left(0\right) = x_0 \tag{11}$$

$$y(t) = Cx(t) + Du(t) = \begin{bmatrix} 1 & 0 \end{bmatrix} x(t) + Di(t)$$
$$u(t) = -K_{LQR}\, x(t) \tag{12}$$

where $x(t)$ is the state vector, $\dot{x}(t)$ is derivative of the state vector, $u(t)$ is the input vector and K_{LQR} is LQR gain matrix that minimises the cost function J.

$$J = \int_0^\infty \left(x^T Q x + u^{\mathrm{T}} R u\right) dt \tag{13}$$

Considering LQI control, it contains a simple state feedback system used in LQR in addition there is output feedback by an integrator that allows servo reference tracking properties [54], and it can be a proper optimal controller for precision control of the swept-back angle. In LQI control, the error is defined as the state of the system and then, the state equation model of the system including the integrator is formed. Thus, steady state errors do not occur since the integral effect will be added to the output error. By this way, the error robustly tends to zero as quickly as possible, assuring robustness of tracking ability. Therefore, the controller has better performance especially against constant disturbances

[54–56]. The matrices of dynamic system, A and B rearranged as $\hat{A}$ and $\hat{B}$, and are given in Equation (14), respectively.

$$\hat{A} = \begin{bmatrix} A & 0 \\ -C & 0 \end{bmatrix}, \ \hat{B} = \begin{bmatrix} B \\ 0 \end{bmatrix} \tag{14}$$

$$u(t) = -K_{LQI}\, z(t) = -K_{LQI} \begin{bmatrix} x \\ x_i \end{bmatrix} \tag{15}$$

For sliding mode control (SMC), it can change the dynamics of a nonlinear system by applying a discontinuous control signal. The discontinuous control signal enforces the system to slide along sliding surface. Considering the SMC characteristics, it can be claimed that system performance has insensitivity to parameter variations, and thus, could result in complete rejection of disturbances [57, 58]. Therefore, it is a suitable controller for FWS, which operates under uncertainty and external disturbance.

Although SMC is a robust controller, the sliding mode has disadvantages such as the chattering phenomenon [59, 60]. In fact, a number of analytical design methods were proposed to overcome the effects of the chattering [59, 61–63]. For instance, one approach to reduce the chattering involves replacement of signum function with a high gain saturation function [59]. Another approach is based on introducing observers for the unmodeled part of the system [61]. The third approach is to design a higher order sliding mode controller to retain the robustness, and thus, eliminating the chattering [62–64]. In this study, we, first, preferred to use the saturation function due primarily to its simplicity, and the plant is considered to be a single-input second-order linear model as given in Equation (16):

$$\ddot{x}(t) = -(A + \Delta A)\,\dot{x} - (B + \Delta B)\,x + (C + \Delta C)\,u(t) + d(t) \tag{16}$$

where A, B and C are nominal system parameters, ΔA, ΔB and ΔC are unknown model uncertainties introduced due to the plant parameters, nonlinear friction, and unmodeled dynamics, and d(t) is external disturbance of the system. In this case, $A = -\frac{B_{eq}}{J_{eq}}$, $B = 0$ and $C = \frac{K_t}{J_{eq}}$. The lumped uncertainty satisfies $|D| \leq D_{max}$ condition, is bounded, unknown, denoted with $D\,(t, u(t))$, and is given below:

$$D\,(t, u(t)) = \pm \Delta A \dot{x} \pm \Delta B x \pm \Delta C u(t) + d(t) \tag{17}$$

Then, Equation (16) can be rewritten as

$$\ddot{x}(t) = -A\dot{x} - Bx + Cu(t) + D\,(t, u(t)) \tag{18}$$

The upper bound for the uncertainty D_{max} is member of positive real constants R^+, and is given by

$$D_{max} = \Delta A\,|\dot{x}| + \Delta B\,|x| + \Delta C \bar{u}(t) + |d(t)| \tag{19}$$

where $\bar{u}$ is the input hard constraint $|u(t)| \leq \bar{u}$. In sliding mode, the purpose of the control is to specify a control input, u(t), such that the tracking error, e(t), converges to zero when the closed-loop system follows the desired trajectory. SMC enforces the error to approach the sliding manifold, and then error moves along the origin. The tracking error e and its derivatives are defined in Equation (20), where, x_d refers to the desired position.

$$e(t) = x_d(t) - x(t)\,, \ \dot{e}(t) = \dot{x}_d(t) - \dot{x}(t)\,, \ \ddot{e}(t) = \ddot{x}_d(t) - \ddot{x}(t) \tag{20}$$

When time goes to infinity, error should converge to zero, therefore, s must be a stable sliding surface; only then the error will die out asymptotically. This means that the desired reference trajectory can be followed asymptotically [65]. The sliding surface variable, s, is defined as [66]

$$s(t) = \left(\lambda + \frac{d}{dt}\right)^2 \int e(t)dt = \lambda^2 \int e(t)dt + 2\lambda e(t) + \dot{e}(t), \ \ \lambda \in R^+ \tag{21}$$

$$\dot{s}(t) = \lambda^2 e(t) + 2\lambda \dot{e}(t) + \ddot{e}(t)$$

$$\dot{s}(t) = \left(\ddot{x}_d(t) + A\dot{x}(t) + Bx\,(t) - Cu(t) - D\,(t, u(t)) + \lambda^2 e(t) + 2\lambda \dot{e}(t)\right) \tag{22}$$

The process of sliding mode control includes two separate phases, one of which is known as sliding phase, and is considered when "s(t) = 0" and "$\dot{s}$(t) = 0". The second phase is the reaching phase, which is used when "s(t) $\neq$ 0". The control laws (i.e., equivalent control, switching control) are derived for each of these phases [65]. The *equivalent control* is described when the trajectory of states is near a sliding surface (s = 0), and is obtained from Equation (20). Also, it is represented by u_{eq}, and is arranged to cancel out known terms as [65–67]:

$$u_{eq}(t) = \frac{1}{C}\left(\ddot{x}_d(t) + A\dot{x}(t) + Bx(t) + \lambda^2 e(t) + 2\lambda\dot{e}(t)\right) \tag{23}$$

The switching control is introduced to deal with matching uncertainties and disturbances, and symbolised with u_{sw} [65–68]:

$$u_{sw}(t) = -k\,sign\,(s(t)) \tag{24}$$

where, k is a positive constant, $k \in R^+$, and to dominate uncertainty and disturbance, k must be properly selected to satisfy $k > D_{max}$. Reaching condition is known as fundamental inequality in sliding mode and can be given as $s(t)\dot{s}(t) < 0$ [66, 67, 69]. Considering the plant with uncertainties and disturbances given in Equation (16) and to satisfy reaching condition, the control input signal $u(t)$ could be designed as given below:

$$u(t) = u_{eq}(t) + u_{sw}(t) \tag{25}$$

If Equation (24) is substituted into Equation (22), one has:

$$\dot{s}(t) = (-k\,sign\,(s(t)) - D\,(t, u(t))) \tag{26}$$

To avoid chattering, saturation function Equation (27) can also be used instead of the signum function Equation (24) [65].

$$sat\left(\frac{s}{\alpha}\right) = \begin{cases} \dfrac{s}{\alpha} \; if \; \left|\dfrac{s}{\alpha}\right| < 1 \\ sign\left(\dfrac{s}{\alpha}\right) \; if \; \left|\dfrac{s}{\alpha}\right| \geqslant 1 \end{cases} \tag{27}$$

$$u = u_{eq} - k\frac{s(t)}{|s(t)| + \alpha} \tag{28}$$

where α and k are positive constants and α is defined as the thickness of the boundary layer.

Briefly, the value of continuous input signal changes between $\pm$k. Thus, in this study, the switching control has the modified saturation function Equation (28).

Regarding second-order sliding mode control, it is implemented to overcome the chattering phenomenon, as also afore-mentioned as the third approach for this purpose in SMC. In fact, SOSMC provides smooth control and better performance in the practice with less chattering while preserving the robustness properties [67]. In the particular case of the SOSMC, the aim of the controller is to steer to zero both the sliding variable s and its first-order time derivative in a finite time (as $s(t) = \dot{s}(t) = 0$) [70]. In the literature, there are a number of sliding surfaces generated for SOSMC such as integral sliding surface [71, 72], PID sliding surface with two independent gain parameters [57], and PID sliding surface with three gain parameters [67]. In the present case, sliding surface is defined as:

$$\dot{s}(t) + \beta_c s(t) = \left(\lambda + \frac{d}{dt}\right)^2 \int e(t)dt, \; \lambda \in R^+ \tag{29}$$

$$\dot{s}(t) + \beta_c s(t) = \lambda^2 \int e(t)dt + 2\lambda e(t) + \dot{e}(t) \tag{30}$$

$$\ddot{s}(t) + \beta_c \dot{s}(t) = \lambda^2 e(t) + 2\lambda\dot{e}(t) + \ddot{e}(t) \tag{31}$$

where λ is an independent parameter gain which is related to error, and the gain parameter of sliding surface, β_c, which is a positive constant, $\beta_c \in R^+$, contributes to the damping of s(t). The $D\,(t, u(t))$, which

was also given in Equation (17), denotes the lumped uncertainty. When the second order derivative of the error, which was also given in Equation (20), substitutes into Equation (31), we can rewrite the equation as follows:

$$\dddot{s}(t) + \beta_c \dot{s}(t) = \lambda^2 e(t) + 2\lambda \dot{e}(t) + \ddot{x}_d(t) + A\dot{x}(t) + Bx(t) - Cu(t) - D(t, u(t)) \tag{32}$$

When the system is on the sliding manifold, the error, e(t), will converge to zero exponentially if the coefficient λ is chosen properly. If the limit of the error goes to zero in infinite time, $\lim_{t \to \infty} e(t) = 0$, it means that the system is asymptotic stable. Moreover, $\ddot{s}(t) = 0$ is recognised as an essential condition for the error to stay on the sliding manifold. With this assumption, the equivalent control is formed as given in Equation (33), and disturbances are not taken into account for the equivalent control since the nominal system model is assumed known.

$$u_{eq} = \frac{1}{C} \left(\ddot{x}_d(t) + \lambda^2 e + 2\lambda \dot{e} + A\dot{x}(t) + Bx(t) - \beta_c \dot{s} \right) \tag{33}$$

In our case, the switching control is introduced with saturation function as:

$$u_{sw} = \lambda_2 s(t) + k_s sat(\dot{s}(t)) \tag{34}$$

where λ_2 and $k_s \in R^+$ with $\lambda_2 > \frac{1}{C}$ and $k_s > \frac{D_{max}}{C}$ with $D_{max} = \sup_{\forall t, s, \dot{s}=0} D(t, u(t))$. When Equations (33) and (36) are substituted into Equation (32), the final equation becomes:

$$\ddot{s} = -D(t, u(t)) - C\lambda_2 s(t) - Ck_s sign(\dot{s}(t)) \tag{35}$$

It is known that the stability is assured if the derivative of the Lyapunov function $\dot{V}$ is a negative definite. Thus, the Lyapunov function is chosen as given in Equation (36) to guarantee stability:

$$V = \frac{1}{2} s(t)^2 + \frac{1}{2} \dot{s}(t)^2 \text{ with } V(0) = 0, \ s(t) \neq 0, \ \dot{s}(t) \neq 0 \tag{36}$$

If taking the first-time derivative of Equation (36), and then Equation (35) substituted into it, one has:

$$\begin{aligned}
\dot{V} &= s(t)\dot{s}(t) + \dot{s}(t)\ddot{s}(t) \\
&= s(t)\dot{s}(t) + \dot{s}(t)(-D(t, u(t)) - C\lambda_2 s(t) - Ck_s sign(\dot{s}(t)) \\
&= s(t)\dot{s}(t) - \dot{s}(t)D(t, u(t)) - C\lambda_2 s(t)\dot{s}(t) - Ck_s |\dot{s}(t)| \\
&\leq |\dot{s}(t)| (s(t) - C\lambda_2 s(t) - D(t, u(t)) - Ck_s) \\
&\leq |\dot{s}(t)| (|s(t)| - C\lambda_2 |s(t)| - D(t, u(t)) - Ck_s) \\
&\leq |\dot{s}(t)| (|s(t)| - C\lambda_2 |s(t)| + D_{max}(t, u(t)) - Ck_s) \\
&= -|\dot{s}(t)| (|s(t)| (C\lambda_2 - 1) - D_{max}(t, u(t)) + Ck_s) < 0.
\end{aligned} \tag{37}$$

Hence, from the above analysis, the global asymptotic stability is assured since $s(t) \neq 0$, $\dot{s}(t) \neq 0$, $k_s > \frac{D_{max}}{C}$, $\lambda_2 > \frac{1}{C}$, $|s(t)| > 0$, $|\dot{s}(t)| > 0$, and thus, it can be proved that $\dot{V} < 0$. The requirement of satisfying $k_s > \frac{D_{max}}{C}$ is obligatory to dominate the matching uncertainties.

2.4 System compositions and working principle

The FWS considered here consists of a slider-crank mechanism and motor assembly. Motor component assembly consists of encoder, gearbox, screw and BLDC motor. A gearbox is introduced to improve the output torque and BLDC motor position is measured by rotary encoder. Regarding control, LQR, LQI, sliding mode and second-order sliding mode controllers were tested to adjust the swept-back angle through BLDC motor position. The real-time controller responses were examined under aerodynamic disturbances that linearly vary with swept-back angle. In fact, these aerodynamic disturbances were
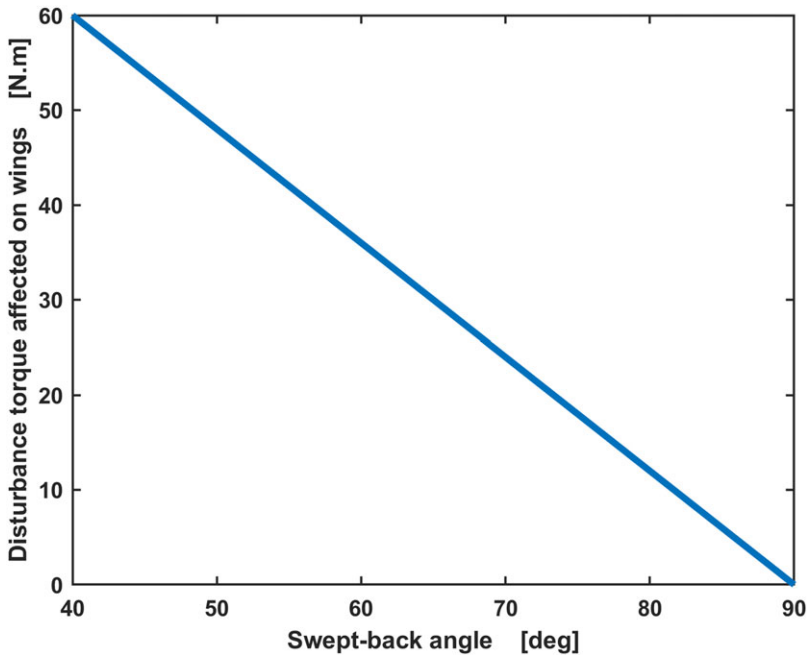
Figure 5. *Variation of disturbance torque versus swept-back angle.*

implemented by extension springs which were attached to wings. The extension springs were carefully chosen and manufactured with specific properties to provide more moment than encountered in flight. They were placed inside the protection case owing to security reasons and were mounted to wings with these aluminum casing. The extension springs were manufactured properly with 17.4 active coils of 3.8 mm diameter wire to provide a spring coefficient of 3.73. The test system was designed as while decreasing of the swept-back angle, the value of aerodynamic disturbance torque increases as shown in Fig. 5.

In selection of the system components, kinematic and dynamic analyses were taken into account. The maximum value of the net force on the slider might approach about 10^3 N, and thus, safety should be provided with proper screw selection. Maxon spindle drive component, consisting of a ball-screw, 1:3.7 reducer, and a rotary incremental encoder was chosen to meet the system requirements. Regarding the motor and encoder, it can be seen from Fig. 3b that the motor must accomplish a minimum of 780 mNm torque.

The kinematic and dynamic analysis, as well as the system identification and controller design were all conducted with MATLAB. Following the assembly, the system identification process was performed, and then the developed controllers were applied to the presented system. Data collection and transfer processes between host and target were conducted using a NI PCI-6221 data acquisition card working with 1 kHz sample time via MATLAB xPC Target toolbox (Fig. 6). The BLDC motor was driven by an AMC motor driver. Briefly, the system is controlled by adjusting the current output and the current direction through the motor driver.

3.0 Results and discussions

Input signal selection is the initial step of system identification [43]. When implementing the system identification, the slider was brought to its strokes midpoint. The movement of the system is restricted by mechanical limits, so the input signal PRBS should also be limited by its frequency and amplitude. During the system identification, it was observed that a PRBS signal with 30 Hz frequency and
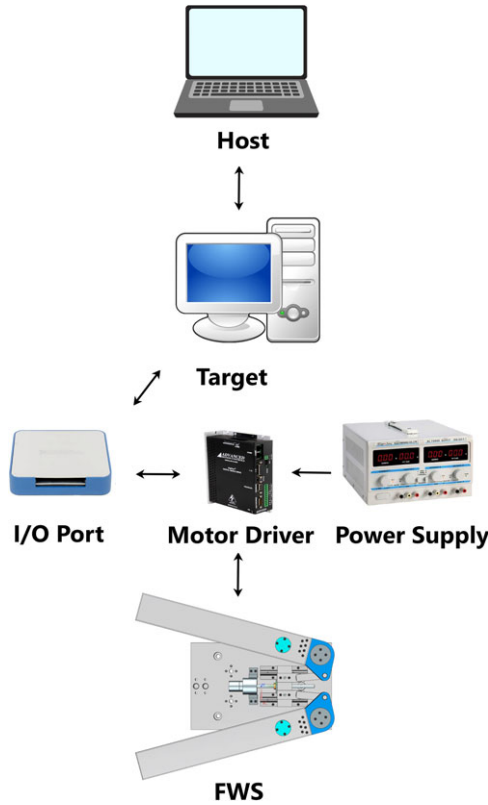
Figure 6. *The diagram of xPC Target and data acquisition system.*

2A amplitude should be enough, not only to avoid any reverse effects on FWS, but also to oscillate at the entire stroke of the slider. Figure 7a illustrates PRBS signal as an input signal and swept-back angle as an output signal. Figure 7b shows PRBS power spectral density (PSD).

Another important point in system identification is the validation of models, which means checking whether the predicted model matches the system model. When performing the system identification, the FWS model was estimated with the BJ approach, and it must be carefully considered that any predicted model can never be better than an actual system model. Variance accounted for (VAF) is frequently utilised to verify the precision of a model [47]. It is calculated by the following equation Equation (38), where (t) and $\hat{y}(t)$ represents measured and estimated data, respectively.

$$VAF = \left(1 - \frac{VAR\,(y(t) - \tilde{y}(t))}{VAR\,(y(t))} \right) x100 \tag{38}$$

The highest VAF ratio of the system model and its discrete and continuous forms were presented in Table 1. In fact, the discrete time system model is estimated by using the discrete PRBS signal, and then the continuous time model is obtained from the discrete time model by using the bilinear (Tustin) approximation. All controllers are designed according to the continuous system model given in Table 1. Figure 8 shows response of the estimated model and the physical FWS to PRBS signal. The outputs of FWS and estimated model are shown as the swept-back angle.

Following the system identification, we focused on designing the controllers as explained in the material and methods section. The controller design initiates with determining the system performance requirement. The controller should satisfy system performance requirements and the performance of the controller is examined with design characteristics such as rising time, settling time, steady-state

Table 1. *Estimated system model*

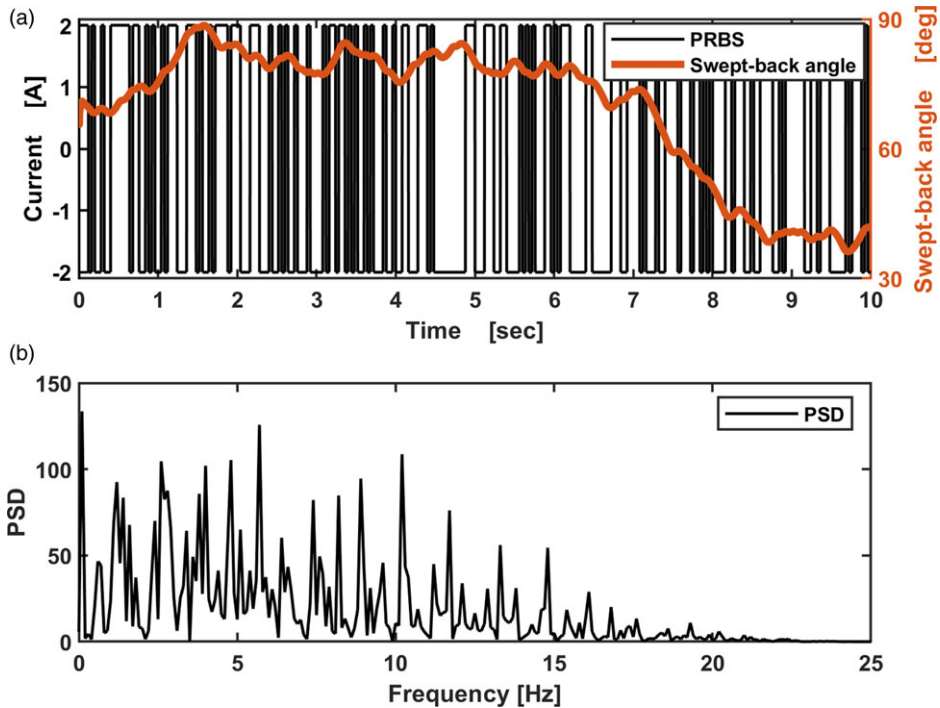| Estimated Discrete Time Model	Estimated Continuous Time Model	VAF %
$\dfrac{0.1826z^{-1}}{1 - 1.9866z^{-1} + 0.9866z^{-2}}$	$\dfrac{13627}{0.0741s^2 + s}$	90.1

Figure 7. *Demonstration of PRBS signal: swept-back angle against input current (a) and power density spectrum of PRBS signal (b).*

error and so on [73]. Furthermore, when rising time decreases, the controller responds more quickly. However, shorter rising times could cause larger overshoot. Briefly, one should consider these impacts in designing a linear controller and can perform these by arranging elements of Q and R matrices properly. In this study, controller parameters are deliberately chosen in a specific range based on specifications of definite general-purpose bombs and their mission requirements, which we will explain later in more detail. In other words, the elements of Q and R, which are design matrices of LQR and LQI (Equation (39) and (40) respectively) were selected as:

$$Q_{LQR} = \begin{bmatrix} 55 & 0 \\ 0 & 0.01 \end{bmatrix}, \; \text{R}_{LQR} = 6000, \tag{39}$$

$$Q_{LQI} = \begin{bmatrix} 180 & 0 & 0 \\ 0 & 0.01 & 0 \\ 0 & 0 & 1000000 \end{bmatrix}, R_{LRI} = 100000 \tag{40}$$

On the other hand, SMC and SOSMC are nonlinear controllers, thus, their design characteristics can not be formulated like linear controllers. Appropriate controller gains were arranged in MATLAB Simulink simulations to meet system requirements. Therefore, the ramp signal was implemented to SMC and SOSMC controllers, and thus, system characteristics were determined from controllers' responses.

Table 2. *Bandwidth of each controller*

	LQR	LQI	SMC	SOSMC
Bandwidth [rad/s]	58.4	55.5	69.1	68.5
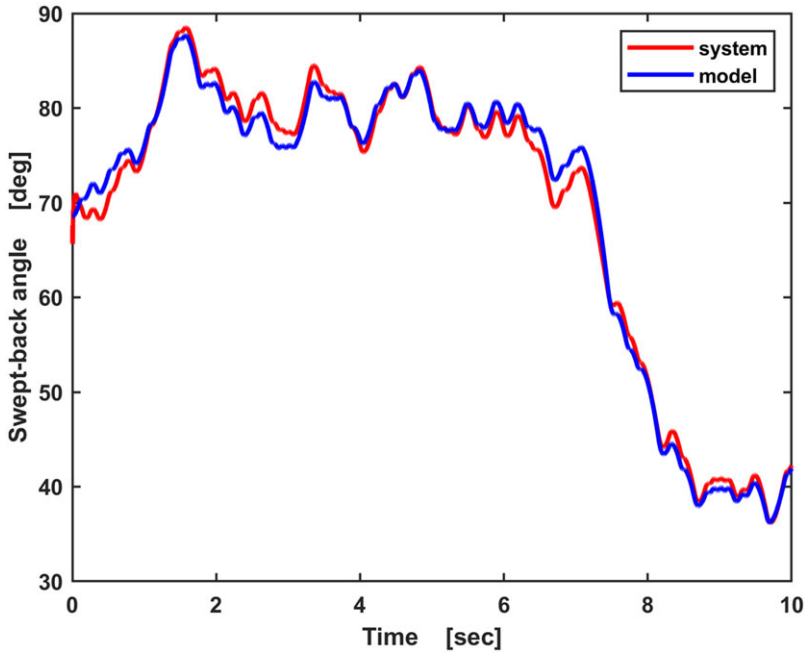
Figure 8. *Validation of measured output and estimated model.*

The slope of the ramp signal was adjusted from 90° to 40° in one second. Besides, in simulation, bandwidths of nonlinear and linear controllers were calculated as listed in Table 2 by applying a Chirp signal, which possess a linearly arising frequency between 0,1 and 100 Hz. The bandwidth of a controller refers to its capability to track and respond to changes in the input reference signal or disturbances within a specific frequency range. A wider bandwidth is generally an indicator of a faster response and better tracking performance. The performance metrics of the controllers (Table 2) are critical regarding their effectiveness in terms of meeting application-specific requirements. The bandwidths of the controllers are selected in such a way that they are close to each other, and hence, allowing a fair comparison of their performances under similar conditions. This approach ensures that the influence of bandwidth differences on the controller performance is minimised, allowing a more accurate evaluation of other performance metrics. By selecting comparable bandwidth values, we can specifically assess and compare other important aspects of the controllers, such as SSE, delay, chattering and energy consumption.

In fact, the controller is expected to follow the reference input with a minimum SSE, as well as to achieve this by responding with a minimum energy consumption. SMC parameters were selected for this purpose as $k = 1200000$, $\lambda = 120$, while SOSMC parameters were chosen as $k_s = 700$, $\lambda = 120$, $\lambda_2 = 7$, $\beta_c = 100000$.

In real-time experiments, the responses of each controller to the ramp input signal (40-degree slope) were collected and these data were used to calculate the system characteristics. These experiments were performed on each controller to test the behaviour of controllers under both aerodynamic loads and in the absence of any disturbances. The controller parameters were chosen properly according to mission requirements of specific general-purpose bombs considering the bomb, and the wings of FWS are exposed to aerodynamic loads based on expertise of an institute working on development of bombs

and such kits for about 50 years. Specifically, the foldable wings in the present work should be able to operate under 60 N.m (i.e., second flight scenario in the manuscript) aerodynamic loads with a SSE of <0.2°, settling time should be less than 120 ms, and the wings should be rapidly controlled within 1 s between 40° and 90°. Also, the bandwidths of each controller are chosen in a range of 55∼70 rad/sec to satisfy afore-mentioned mission requirements, and to provide a more accurate comparison of robustness and tracking performance between linear and non-linear controllers. The settling time and overshoot are calculated by responses of each controller to 40° input ramp signal adjusted in 1 s, and also rms current of each controller as well as their bandwidth are given in Table 3 (Fig. 9).

The performances of LQR, LQI, SMC and SOSMC were investigated for two different flight scenarios, which were given in Figs 10 and 11. The first generated input reference involves 50° opening of wings in 1 s, and then, change of swept-back angle multiple times during a 10 s period. However, the flight conditions are not static in practice and are open to fluctuations depending on various external factors. In other words, various loads or forces might act on the wings at any time during a mission. Therefore, extension springs were mounted to apply aerodynamic loads to FWS, thus, the second flight scenario was created for the observation of controller performances under various aerodynamic loads. Figure 9 shows the used reference input signal.

Figure 10 shows the reference tracking performances of each controller (a), the tracking errors (b) and instant current consumptions (c) in the absence of disturbance. The results show that all of the controllers successfully adjusted the swept-back angle to open the wings to a desired position of 40° in roughly 1 s. In Fig. 10b, it can be clearly seen that LQR and LQI track the input reference with a delay when the reference input is changed. The results show that the tracking error of LQR can reach 1.38°, while it can reach about 1.70° with LQI. But, as can be seen in zoomed image boxes for 1.44–1.51 s and 4.4–4.6 s, both controllers can follow the reference input with nearly zero SSE when the reference input holds the swept-back angle at constant positions. On the other hand, SMC and SOSMC follow the reference aggressively close. Comparing to the tracking error of linear controllers (LQR and LQI), nonlinear controllers (SMC and SOSMC) respond much faster with fewer tracking errors. Also, they react much better to the sudden changes such as in the case at sixth second of the flight scenario due to their robust design structure. Regarding current consumption, it is plotted in Fig. 10c. FWS inertia effect can be seen at the beginning and end of the movement for each controller, and they require more current to overcome the inertia effect upon encountering any abrupt changes (i.e., starting the motion, changing the direction, etc.). Furthermore, when the wings are at fixed positions, LQR, LQI and SOSMC have nearly zero current consumption, while the chattering effect of SMC is much more prominent as shown in 1.45 s–1.5 s. Moreover, upon comparing LQR with LQI, one could see that both controllers have a similar current consumption trend. Likewise, Fig. 10c suggests that SMC and SOSMC also possess similar current consumption trends among themselves during changing the swept-back angle. However, SMC and SOSMC consume more current than LQR and LQI to quickly respond to abrupt changes in reference signal as can be understood from the rms current results in Table 2. In fact, SMC is found to be the controller with most energy consumption in the absence of disturbances due to the chattering phenomenon. Overall, it can be said that linear controllers (LQR and LQI) might be preferred over non-linear controllers (SMC and SOSMC) for the as-developed FWS in the absence of disturbances.

Figure 11 shows the reference tracking performances of each controller (a), tracking errors (b) and instant current consumptions (c) under varying aerodynamic disturbances (i.e., 60 N.m at 40° – changing with swept-back angle). When the tracking performances of each controller under aerodynamic loads are examined, one can say that all of the controllers except LQR can successfully adjust the swept-back angle to the opened position of 40° in roughly 1 s. Besides, it is seen from Fig. 11b that LQR performs with an SSE of roughly 0.39° at 40° swept-back angle, though LQI, SMC and SOSMC can follow the reference swept-back angle with pretty much zero SSE as shown in Table 2. However, the results suggest that LQR can also successfully follow the reference angle with nearly zero SSE at lower swept-back angles as shown in zoomed image boxes at 4.5 and 4.6 s. This is because the loads on wings vary with swept-back angle, and there will be fewer model uncertainties and disturbances at lower swept-back angles. This suggests that as-designed LQR can deal with model uncertainties and

Table 3. *Real-time experimental results of each controller: in the absence and the presence of aerodynamic loads*

	LQR		LQI		SMC		SOSMC	
	No disturbance	*Under disturbance*	*No disturbance*	*Under disturbance*	*No disturbance*	*Under disturbance*	*No disturbance*	*Under disturbance*
Settling time (%2) [ms]	1,009	1,065	1,017	1,069	981	1,004	981	1,004
Overshoot [deg]	–	–	0.04°	0.17°	0.40°	0.17°	0.43°	0.16°
Steady-state error [deg]	0.003°	0.39°	0°	0.01°	0°	0.05°	0°	0.05°
Rms current [A]	1.17	4.61	1.18	3.97	2.12	4.01	1.95	3.69
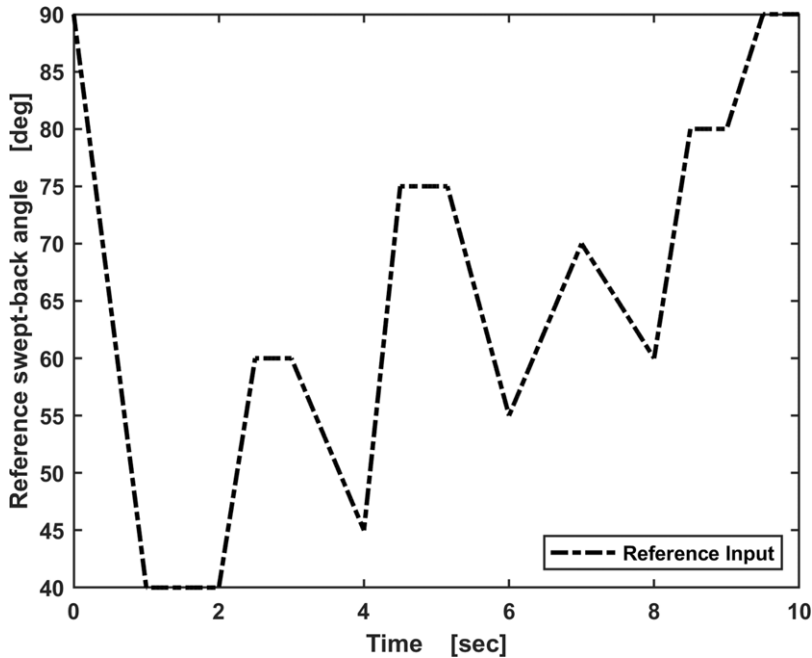
Figure 9. *The generated reference input signal for both flight scenarios.*

disturbances up to a point. Besides, it is important to note that the design matrices of LQR and LQI were properly selected based on afore-mentioned mission and equipment requirements. In this work, LQR provided the lowest SSE under 60 N.m when its Q and R were selected as given in Equation (39). For instance, beyond a R value of more than 6,000, the mechanism uncontrollably trembled and operated with a disturbing noise. Likewise, below a R value of 6,000, the SSE of LQR was higher than 0.39°. In Fig. 11c, under 60 N.m of aerodynamic load, both LQR and LQI initially spend 10 amperes, but, when the tracking error of LQI decreased, then the current consumption of LQI also reduced to 6.5 amperes due to the integrator. However, SMC and SOSMC spend 3 amperes, and 2.7 amperes respectively, under 60 N.m of aerodynamic load as shown in the zoomed image box for 1.41 s–1.5 s. Besides, SMC did not lead to excessive chattering in Fig. 11c due possibly to the presence of extension springs to generate aerodynamics loads. These extension springs might contribute to the elimination of bearing clearances, and thus reducing the risk of chattering. The fact that chattering is observed again to some extent at lower swept-back angles (Fig. 11c) adds credibility to this idea. Moreover, the presence of extension springs caused to reduce overshoot (at 40°) of LQI, SMC and SOSMC, as can be seen in Fig. 11a and Table 2. According to the rms current results in Table 2, it might be said that LQR and LQI consume more energy to overcome model uncertainties and external disturbances. Overall, it can be said that SOSMC might be preferred over other alternatives for the as-developed FWS under 60 N.m (at 40°) of aerodynamic load due to its robustness, tracking performance and efficiency.

Considering both scenarios, LQR optimised gain "K" can only work in a certain operation range and cannot react to system uncertainty. Although LQR and LQI are optimal control techniques, the results show that LQR cannot overcome SSE under relatively higher disturbances. It looks like LQR is not a feasible option in our system, particularly considering the various uncertainties that may arise during practice. On the other hand, we observed that the control input of SMC has the chattering effect in the absence of the disturbance. The chattering leads to oscillating around the sliding surface. Additionally, quick variations in control signals could result in fatigue of mechanical parts, and thus, the system might fail under cyclic loads [74, 75]. Therefore, SMC is not a proper controller for our system, even though the response of SMC is also faster than LQR and LQI. Consequently, LQI and SOSMC pursued the
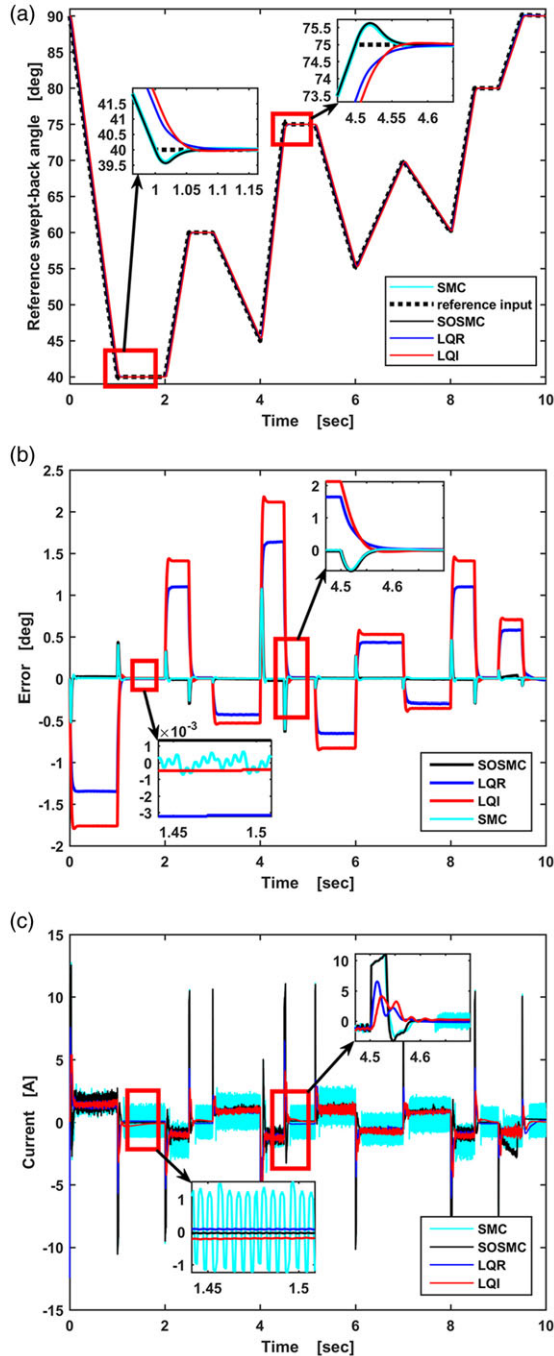
Figure 10. *Real-time experimental results: (a) reference tracking, (b) tracking error and (c) instant motor current of different controllers in the absence of aerodynamic loads.*

reference successfully in the presence of aerodynamic disturbances. Regarding LQI, it is quite efficient especially against maximum value of external disturbance due to integral feedback loop and also this loop reduces the SSE to 0.01°. Besides, the experiments were carried out at room temperature (RT) for each flight scenario. Although LQI has a minimum SSE under disturbances, the developed system
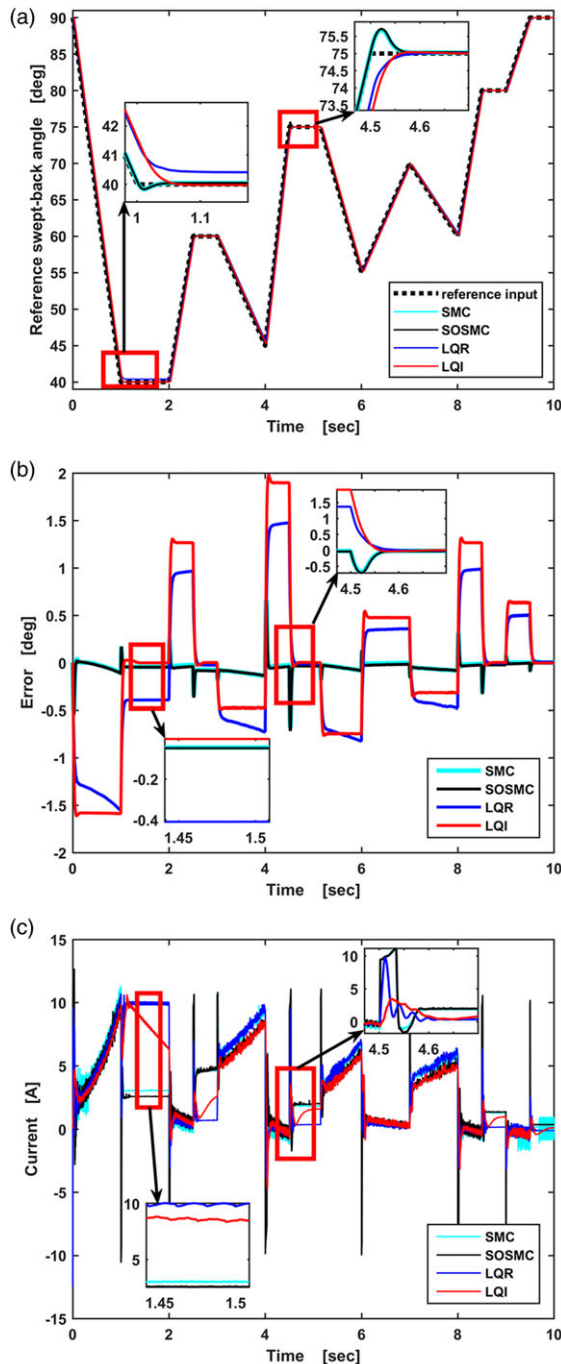
Figure 11. *Real-time experimental results: (a) reference tracking, (b) tracking error and (c) instant motor current of different controllers in the presence of aerodynamic loads (i.e., 60 N.m at 40° – changing with swept-back angle).*

might fly in a mission at much lower temperatures than RT. In this case, the system model of FWS might change, and thus, this will necessitate fresh arrangement of LQI gain matrix, K. On the other hand, it is known that SOSMC can successfully pursue the reference in the presence of disturbances due to its

higher insensitivity to the variation of parameters and rapid response times without depending on the external disturbances [76]. Although SOSMC operates with a SSE of 0.05°, which is worse than LQI, under 60 N.m (at 40°) disturbance, this is acceptable for current operating requirements. SOSMC not only consumes less current but also follows the reference swept-back angle more aggressively as shown in Fig. 11 and Table 2. These whole situations are ascribed to the fact that the SOSMC input signal "u_{sw}", is designed by taking model uncertainties into account since uncertainties and disturbances are already included in the switching control input.

4.0 Conclusion

To sum up, a novel folding wing kit is developed for guided ammunitions. In contrast to previous wing kits, the as-developed FWS provides a folding functionality and there are not any fixing mechanisms or brake elements for fixing of wing position. Instead, various controllers were designed to adjust and hold the desired swept-back angles. The presented FWS can adjust the swept-back angle between 40° and 90° in 1 s during the flight. By this way, the swept-back angle can be quickly adjusted to 90° during the terminal phase to solve the drag problem on wing kits during diving, and thus, the risk of change on the angle-of-attack is minimised. Besides, the developed FWS can also be used in adjusting the swept-back angle during gliding phase to adapt ammunition to any unexpected conditions that may arise during a mission. Briefly, we first conducted a mechanism design with dynamic and kinematic analysis. Then, the designed components of the system are manufactured following material selection, and the FWS was assembled. Following this, system identification was implemented with the Box-Jenkins approach and the precision of the estimated model was verified by VAF as % 90.1. Regarding control, LQR, LQI, SMC and SOSMC were designed to adjust and to hold the swept-back angle to desired positions without any brake or fixing mechanism. To compare the performances of controllers, two flight scenarios were generated. In the absence of disturbance, the real-time results show that each controller was able to follow the reference input, while LQR has much better response and lower energy consumption than the others. In the presence of aerodynamic disturbances, SOSMC provided best results considering reference tracking, robustness as well as energy consumption, as discussed thoroughly in the manuscript.

Competing interests. The authors declare that they have no competing interests.

References

[1] Hallion R.P. *Precision Guided Munitions and the New Era of Warfare*. Australia: Air Power Studies Centre, Royal Australian Air Force, 1997.

[2] Maini A.K. *Precision Guided Munitions, in Handbook of Defence Electronics and Optronics: Fundamentals, Technologies and Systems*. India: John Wiley & Sons Ltd., 2018, pp. 933–1011.

[3] Lund F. Evolution of navy air-to-surface guided weapons. In *41st Aerospace Sciences Meeting and Exhibit*, Reno, Nevada, 2003, p 291.

[4] Sreeja S. and Hablani H. Precision munition guidance and estimation of target position in 2-D. In *AIAA Guidance, Navigation, and Control Conference*. American Institute of Aeronautics and Astronautics, Inc, San Diego, CA, USA, 2016, pp 1–19.

[5] Hoehn J. and Ryder S. *Precision Guided Munitions Background and Issues for Congress*: Congressional Research Service, 2020. https://apps.dtic.mil/sti/citations/AD1169867

[6] Kowaleczko G. and Pietraszek M. Estimation of the accuracy of laser guided bomb. *J. KONES*, 2016, **23**, pp 271–279.

[7] Martin L. *Paveway II Plus Laser Guided Bomb (LGB)*, (2022). https://www.lockheedmartin.com/en-us/products/paveway-ii-plus-laser-guided-bomb.html

[8] Mouada T., Pavic M.V., Pavkovic B.M. et al. Application of optimal control law to laser guided bomb. *Aeronaut. J.*, 2018, **122**, (1251), pp 785–797.

[9] TÜBİTAK-SAGE. *Precision Guidance Kit (HGK)*, (2022). http://www.sage.tubitak.gov.tr/tr/urunler/hassas-gudum-kiti-hgk

[10] Aselsan. Laser Guidance Kit (LGK), 2022. https://www.aselsan.com.tr/tr/cozumlerimiz/insansiz-sistemleri/lgk-lazer-gudum-kiti

[11] Boeing. *Joint Direct Attack Munition Extended Range (JDAM-ER)*, (2022). https://www.ferra-group.com/capabilities/research-development/ (accessed 26 March 2022).

[12] TÜBİTAK-SAGE. *Wing Assisted Guidance Kit (WGK)*, 2022. http://www.sage.tubitak.gov.tr/tr/urunler/kanatli-gudum-kiti-hgk

[13] Boeing. *Joint Direct Attack Munition Extended Range (JDAM-ER)*, (2022). https://www.ferra-group.com/capabilities/research-development/

[14] Harris G.L. and Levy N.A. *Device for Extending the Range of Guided Bombs*, 2000, The United States Patent and Trademark Office US6152041A. https://patents.google.com/patent/US6152041A/en

[15] Harris G.L. *Air Launched Munition Range Extension System and Method*, 1992, The United States Patent and Trademark Office US5141175. https://patents.google.com/patent/US5141175A/en

[16] Shmoldas J.D., Hutchings M.B. and Barlow C.W. *Extendable Wing for Guided Missiles and Munitions*, 1997, The United States Patent and Trademark Office US5615846A. https://patents.google.com/patent/US5615846A/en?oq=US+5%2c615%2c846

[17] Shai M. *Air Vehicle and Deployable Wing Arrangement Therefor*, 2008. World Intellectual Property Organization WO2008010226A1. https://patents.google.com/patent/WO2008010226A1/en?oq=WO2008010226A1

[18] Qingsheng L., et al. *Wing Folding Mechanism Based on Flex-Wing Aircraft*, 2014, China National Intellectual Property Administration CN103661919. https://patents.google.com/patent/CN103661919A/en

[19] Bouchard M.L., Gogineni P., Eisentraut R.A. et al. *Winged Vehicle with Variable-Sweep Cantilevered Wing Mounted on a Translating Wing-Support Body*, 2007, The United States Patent and Trademark Office US7185847B1. https://patents.google.com/patent/US7185847B1/en

[20] Chen Z. *Spacecraft and Aerospace Plane Having Scissors Wings*, 2004, The United States Patent and Trademark Office US6745979B1. https://patents.google.com/patent/US6745979B1/en?oq=US6745979

[21] Garrett T.M. *Aerodynamic Body Having Coplanar Joined Wings*, 1999, The United States Patent and Trademark Office US5899410A. https://patents.google.com/patent/US5899410A/en?oq=us5%2c899%2c410

[22] Niemeyer T., Schwies M.D., Naderhoff U. et al. *Guide Assembly for a Missile*, 2004, The United States Patent and Trademark Office US6758435B2. https://patents.google.com/patent/US6758435B2/en

[23] Spanovich J.P. *Variable Alignment Mechanism*, 1991, The United States Patent and Trademark Office US5671899. https://patents.google.com/patent/US5035378A/en

[24] Wenzel H.A. *Multi-Winged Lifting Body Aircraft*, 1979, The United States Patent and Trademark Office US4146199. https://patents.google.com/patent/US4146199A/en?oq=US4146199

[25] O'Shea H. *Aerial Vehicle with Variable Aspect Ratio Deployable Wings*, 2010, The United States Patent and Trademark Office US7841559. https://patents.google.com/patent/US7841559B1/en

[26] Zarchan P. *Tactical and Strategic Missile Guidance*, 6th ed., Vol. 239. Virginia, USA: American Institute of Aeronautics and Astronautics, 2012.

[27] Shneydor N.A. *Missile Guidance and Pursuit: Kinematics, Dynamics and Control*. West Sussex, England: Horwood Publishing Limited, 1998.

[28] Voskuijl M. Performance analysis and design of loitering munitions: a comprehensive technical survey of recent developments. *Def. Technol.*, 2022, **18**, (3), pp 325–343.

[29] Teope K.I., Jensen D.L., Fortney E.M. et al. Reconfigurable internal weapons carriage system for small fighter aircraft. In *55th AIAA Aerospace Sciences Meeting*. Grapevine, Texas, USA: AIAA, 2017, pp 1–11

[30] Rogers J. and Costello M. Design of a roll-stabilized mortar projectile with reciprocating canards. *J. Guid. Control Dyn.*, 2010, **33**, pp 1026–1034.

[31] Myers G.G. *Folding Wing Structure with a Flexible Cover*, 1993, The United States Patent and Trademark Office US5240203A. https://patents.google.com/patent/US5240203A/en

[32] Svensson N.B. *Folding fins for Missiles*, 1972, The United States Patent and Trademark Office US3650496. https://patents.google.com/patent/US3650496A/en

[33] Vainshtein A. and Bouhryakov A. *Wing Deployment Mechanism*, 2017, The United States Patent and Trademark Office US9689650B2. https://patents.google.com/patent/US9689650B2/en

[34] Rothenhofer G., Walsh C. and Slocum A. Transmission ratio based analysis and robust design of mechanisms. *Precis. Eng.*, 2010, **34**, pp 790–797.

[35] Uicker J.J., Pennock G.R., Shigley J.E. et al. *Theory of Machines and Mechanisms*. Vol. 768. New York, USA: Oxford University Press, 2003.

[36] Söylemez E. *Mechanisms*, 5th ed. Ankara, TR: ODTÜ Yayınları, 2009.

[37] Akgul B., Erden F. and Ozbay S. Porous Cu/Al composites for cost-effective thermal management. *Powder Technol.*, 2021, **391**, pp 11–19.

[38] Krishnan R. *Permanent Magnet Synchronous and Brushless DC Motor Drives*. Florida, USA: CRC Press, 2017.

[39] Pindoriya R.M., Pindoriya R., Mishra A., Rajpurohit B. et al. An analysis of vibration and acoustic noise of BLDC motor drive. In *2018 IEEE Power & Energy Society General Meeting (PESGM)*. Portland, OR, USA: IEEE, 2018, pp 1–5.

[40] Krishnan T.V.D., Krishnan C.M.C. and Vittal K.P. Design of robust H-infinity speed controller for high performance BLDC servo drive. In *2017 International Conference on Smart grids, Power and Advanced Control Engineering (ICSPACE)*. Bangalore, India: IEEE, 2017, pp 37–42.

[41] Shanmugasundram R., Zakariah K.M. and Yadaiah N. Implementation and performance analysis of digital controllers for brushless DC motor drives. *IEEE/ASME Trans. Mechatron.*, 2012, **19**, (1), pp 213–224.

[42] Karnopp D.C., Margolis D.L. and Rosenberg R.C. *System Dynamics: Modeling, Simulation, and Control of Mechatronic Systems*, 5th ed. Hoboken, New Jersey, USA: John Wiley & Sons, 2012.

[43] Soares D. and Serpa A.L. An evaluation of the influence of Eigensystem Realization Algorithm settings on multiple input multiple output system identification. *J. Vib. Control*, 2021, **0**, (0), pp 1–16.

[44] Vuojolainen J., Nevaranta N., Jastrzebski R. et al. Comparison of excitation signals in active magnetic bearing system identification. *Model. Identif. Control*, 2017, pp 123–133.

[45] Vermeulen H.J., Strauss J.M. and Shikoana V. Online estimation of synchronous generator parameters using PRBS perturbations. *IEEE Trans. Power Syst.*, 2002, **17**, (3), pp 694–700.

[46] Bnhamdoon A., Hanif M. and Akmeliawati R. Identification of a quadcopter autopilot system via Box–Jenkins structure. *Int. J. Dyn. Control*, 2020, **8**, pp 835–850.

[47] Guarin D.L. and Kearney R.E. Identification of a time-varying, Box-Jenkins model of intrinsic joint compliance. *IEEE Trans. Neural Syst. Rehabil. Eng.*, 2017, **25**, pp 1211–1220.

[48] Forssell U. and Ljung L. Identification of unstable systems using output error and Box-Jenkins model structures. In *Proceedings of the 37th IEEE Conference on Decision and Control*. Tampa, FL, USA: IEEE, 1998, pp 3932–3927.

[49] Schoukens J., Rolain Y., Vandersteen G. et al. User friendly Box-Jenkins identification using nonparametric noise models. In *Proceedings of the IEEE Conference on Decision and Control*. Institute of Electrical and Electronics Engineers, Orlando, FL, USA, 2011, pp 2148–2153.

[50] Ljung L. *System Identification Toolbox: User's Guide*. Natick, Massachusetts, USA: MathWorks Incorporated, 1995.

[51] Khalfi J., Boumaaz N., Soulmani A. et al. Box–Jenkins Black-Box modeling of a lithium-ion battery cell based on automotive drive cycle data. *World Electr. Veh. J.*, 2021, **12**, (3), p 102.

[52] Tangirala A.K. *Principles of System Identification: Theory and Practice*. Boca Raton, Florida, USA: CRC Press, 2015.

[53] Shehzad M.F., Bilal A. and Ahmad H. Position & attitude control of an aerial robot (Quadrotor) with intelligent PID and state feedback LQR controller: a comparative approach. In *2019 16th International Bhurban Conference on Applied Sciences and Technology (IBCAST)*. Institute of Electrical and Electronics Engineers, Islamabad, Pakistan, 2019, pp 340–346.

[54] Kisszölgyémi I., Beneda K. and Faltin Z. Linear quadratic integral (LQI) control for a small scale turbojet engine with variable exhaust nozzle. In *2017 International Conference on Military Technologies (ICMT)*. Institute of Electrical and Electronics Engineers, Brno, Czech Republic, 2017, pp 507–513

[55] Seto K., Fuji D., Hiramathu H. et al. Motion and vibration control of three dimensional flexible shaking table using LQI control approach. In *Proceedings of the 2002 American Control Conference (IEEE Cat. No.CH37301)*. Institute of Electrical and Electronics Engineers, Anchorage, AK, USA, 2002, pp 3040–3045.

[56] Altun Y. Çeyrek taşıt aktif süspansiyon sistemi için LQR ve LQI denetleyicilerinin karşılaştırılması. *Gazi Üniversitesi Fen Bilimleri Dergisi Part C: Tasarım ve Teknoloji*, 2017, **5**, (3), pp 61–70.

[57] Young K.D., Utkin V. and Özgüner Ü. A control engineer's guide to sliding mode control. *IEEE Trans. Control Syst. Technol.*, 1999, **7**, pp 32–342.

[58] Liu S., Yan B., Zhang T. et al. Three-dimensional cooperative guidance law for intercepting hypersonic targets. *Aerosp. Sci. Technol.*, 2022, **129**, p 107815.

[59] Lee H. and Utkin V. Chattering suppression methods in sliding mode control systems. *Annu. Rev. Control*, 2007, **31**, (2), pp 179–188.

[60] He S. and Lin D. Sliding mode-based continuous guidance law with terminal angle constraint. *Aeronaut. J.*, 2016, **120**, (1229), pp 1175–1195.

[61] Utkin V. *Sliding Modes in Control and Optimization*. Berlin, DE: Springer, 1992.

[62] Mondal S. and Mahanta C. Nonlinear sliding surface based second order sliding mode controller for uncertain linear systems. *Commun. Nonlinear Sci. Numer. Simulat.*, 2011, **16**, pp 3760–3769.

[63] Bartolini G., Ferrara A. and Usai E. Chattering avoidance by second-order sliding mode control. *IEEE Trans. Automat. Control*, 1998, **43**, (2), pp 241–246.

[64] Liu S., Wang Y., Li Y. et al. Cooperative guidance for active defence based on line-of-sight constraint under a low-speed ratio. *Aeronaut. J.*, 2023, **127**, (1309), pp 491–509.

[65] Eker İ. Sliding mode control with PID sliding surface and experimental application to an electromechanical plant. *ISA Trans.*, 2006, **45**, pp 109–118.

[66] Slotine J.-J.E. and Li W. *Applied Nonlinear Control*, Vol. 199. NJ, USA: Prentice Hall, 1991.

[67] Eker I. Second-order sliding mode control with experimental application. *ISA Trans.*, 2010, **49**, (3), pp. 394–405.

[68] Fei J. A class of adaptive sliding mode controller with integral sliding surface. In *2009 International Conference on Mechatronics and Automation*. Changchun, Jilin, China: IEEE, 2009, pp 1156–1161.

[69] Saeed Z. and Soltanpour M.R. The position control of the ball and beam system using state-disturbance observe-based adaptive fuzzy sliding mode control in presence of matched and mismatched uncertainties. *Mech. Syst. Signal Process.*, 2021, **150**, p. 107243.

[70] Capisani L.M., Ferrara A. and Magnani L. Design and experimental validation of a second-order sliding-mode motion controller for robot manipulators. *Int. J. Control*, 2009, **82**, (2), pp 365–377.

[71] Camacho O., Rojas R. and García-Gabín W. Some long time delay sliding mode control approaches. *ISA Trans.*, 2007, **46**, (1), pp 95–101.

[72] Yorgancıoğlu F. and Kömürcügil H. Single-input fuzzy-like moving sliding surface approach to the sliding mode control. *Electric. Eng.*, 2008, **90**, (3), pp 199–207.

[73] Sharma S. and Agarwal K.L. *Intelligent Energy Management Technologies*, M.S. Uddin, et al., Editors. Singapore: Springer, 2021, pp 343–355.

[74] Bartolini G., Pisano A., Punta E. et al. A survey of applications of second-order sliding mode control to mechanical systems. *Int. J. Control*, 2003, **76**, (9–10), pp 875–892.

[75] Edwards C. and Spurgeon S. *Sliding Mode Control: Theory and Applications*. Padstow, UK: CRC Press, 1998.

[76] Utkin V. Variable structure systems with sliding modes. *IEEE Trans. Automat. Control*, 1977, **22**, (2), pp 212–222.